Microstructure mapping of a friction stir welded AA2050 Al–Li–Cu in the T8 state

F. De Geuser[a]*, B. Malard[a,b] and A. Deschamps[a]

[a]*SIMaP, Grenoble INP-UJF-CNRS, BP 75, 38402 Saint-Martin-d'Heres Cedex, France;*
[b]*CIRIMAT, INPT-ENSIACET, 4 Allée Emile Monso 31030, Toulouse, France*

The heterogeneous precipitate microstructure of a AA2050 Al–Li–Cu in the T8 state after friction stir welding has been mapped by small-angle X-ray scattering (SAXS). 2D resolved maps of the fraction and size of both T_1 platelets precipitates and clusters/GP zones formed at room temperature are provided. TEM micrographs of selected zone confirm the interpretation of SAXS intensities. This microstructure mapping is compared to microhardness mapping and a direct correlation is shown. Short duration heat treatments made in a salt bath help understanding precipitate stability and suggest that the temperature exploration alone explains to a large extent the distribution of the precipitates microstructure across the welded structure.

Keywords: precipitation; FSW; SAXS; Al–Cu–Li alloys

Introduction

Friction stir welding is now a relatively mature technology that enables solid-state joining of aluminium alloys and other materials. In aluminium alloys, it proves to be particularly interesting for high strength, high solute alloys that are difficult to weld by other methods and particularly those containing high levels of Cu. Recently, several detailed review papers have summarized the state of the art of the knowledge on the generation of heat by friction and plastic flow, on the distribution of plastic flow around the welding tool, on the resulting microstructures and on many related properties [1]. When friction stir welded, all precipitation hardening alloys (namely, of the 2000, 6000 and 7000 series), regardless of their initial temper (naturally aged or peak aged), share some common characteristic microstructure evolutions, but also present significant differences. In the weld nugget, the high temperature results in a complete dissolution of the pre-existing precipitates. Coarse precipitates may form upon cooling, depending on the quench sensitivity of the alloy and on the details of the welding conditions that govern the thermal history in the nugget zone: welding speed, weld thickness, thermal contact with the backing plate. In the thermo-mechanically affected zone, relatively coarse precipitates are generally found, in relation to the intermediate temperatures reached (typically about 350 °C) and the presence of plasticity that can accelerate the formation or transformation of precipitates. The behaviour of the heat-affected zone is

*Corresponding author. Email: Frederic.de-geuser@simap.grenoble-inp.fr

much more alloy and temper-dependent as it depends critically on the stability of the microstructure with respect to a temperature spike.

In the last decade, new alloys for aerospace applications have been developed based on the Al–Cu–Li system [2]. Following a composition optimization with respect to the formerly available alloys of this family (e.g. 2195), these alloys present very attractive properties without some of the earlier limitations, such as low temperature ageing [3,4]. These alloys, which currently attract a large interest, rely mostly on the precipitation of the T_1-Al_2CuLi phase to obtain their mechanical properties [5–8]. In the T8 (near peak-aged condition), alloys such as AA2198 containing about 3 wt%Cu and 1 wt%Li contain a high density of very thin T_1 plates of high aspect ratio (1.3 nm thickness vs. approximately 50 nm diameter) [5,9,10]. Although several authors have studied the potentiality of the latest generation of Al–Li–Cu for friction stir welds [11–18], only a limited number of studies are available which characterize their microstructure.

Fonda [19] has observed the distribution of precipitate microstructures across an AA2195 friction stir weld. The alloy, whose initial under-aged temper contained mostly thin T_1 and a few θ' plates, presents in the HAZ and TMAZ a gradual coarsening of these plates until complete dissolution in the nugget, where T_B precipitates form at high temperature and δ' precipitates form at low temperature. Shukla [20,21] studied in detail the evolution of precipitates in friction stir welds of thin sheets of AA2195-T8. They observed different levels of T_1 and θ' dissolution in the HAZ and TMAZ. They measured no appreciable change in the length of the T_1 precipitates in the zones where partial dissolution had taken place, nor any appreciable change in thickness. However, due to the extremely low value of T_1 thickness [9,10,22], a moderate thickness increment may have been difficult to observe. The dissolution of T_1 at the weld centre of a AA2195 in the T8 state was already observed by Chen & Chaturvedi [23].

Cavaliere [14] has studied friction stir welds of AA2198-T851 alloy and shown the presence of θ' and δ' phases in the weld nugget and T_1, θ' and δ' in the HAZ and TMAZ. This presence of δ' phase in this alloy is relatively surprising since the detailed study of precipitation sequence in this alloy by Decreus [5] did not provide evidence of the formation of this phase for this alloy composition (albeit along different thermal treatments). Steuwer and co-workers [24] have mapped by small-angle X-ray scattering (SAXS) the microstructure across a friction stir weld of AA2199-T8 alloy. Their analysis proved some degree of coarsening in the HAZ and TMAZ, associated with the partial dissolution of the T_1 precipitates initially present.

As a result of the spatial variation of temperature and strain history within a weld, the resulting precipitate microstructure is extremely heterogeneous. A large number of studies have relied on transmission electron microscopy (TEM) to describe the precipitate nanostructures in the different zones of friction stir welds. However, owing to the fact that the precipitate microstructure may vary very quickly over a few mm and to the large number of different zones to be characterized, such characterization procedure proves to be extremely time consuming, and it remains difficult to obtain a full picture of the precipitate distribution across a friction stir weld. Several studies have shown that using SAXS with synchrotron light sources made it possible to obtain detailed maps of precipitate distributions (average precipitate size, volume fraction), and this method has been applied several times to friction stir welding [24,25]. However, although the interpretation of small-angle scattering data in systems showing near-spherical shape precipitates is relatively straightforward and leads to high quality precipitate maps, the

situation is more difficult in precipitate systems where precipitates are highly anisotropic. Interpretation using classical tools (such as Guinier radius evaluation) has been carried out in one occurrence and provides a qualitative view of microstructural evolution in welds [24]. However, more advanced data analysis is required if a more quantitative characterization is sought. Recently, a method was proposed to extract quantitative data from SAXS applicable to high aspect ratio precipitate platelets [22]. It relies however on the material being highly textured so that the precipitates are viewed close to edge-on by the X-ray beam. It has been shown in a preliminary study that this situation is not met in friction stir welds where the grain texture is highly variable from one region to another [26].

Alloy AA2050-T8 is particularly suited for medium to thick plate applications [27], and its potential for friction stir welding has been evaluated both in terms of mechanical properties and corrosion behaviour [28]. The aim of the present paper will be to present a detailed characterization of the distribution of precipitates across a friction stir weld of this material. This characterization will be obtained using cross-section mapping by SAXS. A special procedure for extracting the morphological information and volume fraction of precipitates from the SAXS data, suited to the specificity of this alloy system, will be presented, and the quantitative capability of this approach will be shown by comparison with TEM images in a few selected regions. The spatial distribution of precipitates will then be compared to the distribution of hardness and discussed by comparing to that obtained during short duration heat treatments made in a salt bath, so as to reach a better understanding of precipitate stability in this alloy.

Experimental details

The base material consists of AA2050 (Al - 3.5wt% Cu - 1wt% Li with Mg and Ag as main secondary alloying elements) 15 mm plates in the T8 condition (i.e. solution heat treated, quenched, stress relieved, naturally aged and peak aged at 155 °C) as delivered by Constellium Voreppe Research Centre (France). The friction stir welding was performed by EADS IW in Suresnes (France) at 400 rotations per minute with an advancement speed of 200 mm per minute. A threaded pin with 3 flats tool was used. Slices transverse to the welding direction were then mechanically cut (10 mm thick for the microhardness measurements, 1 mm thick for SAXS and TEM).

The microhardness specimen was mirror polished down to 1 μm. The microindentation was performed on a fully automated Wilson Tukon 1102 microindenter from Buhler, with a load of 500 from a Vickers indenter. A total of 1880 indents (20 × 95) separated from 0.65 mm were used to cover a large enough area around the welded structure (13 mm × 60 mm).

The SAXS took place on BM02-D2AM, a French CRG beamline at the ESRF, Grenoble, France. The X-ray energy was 16.128 keV and the beam extension about 200 μm in both direction. The sample to the 2D CCD detector distance was about 600 mm. The SAXS specimen was mechanically grinded to a thickness of 600 μm, which is closed to their X-ray attenuation length at the energy used. There was a ±50-μm thickness variation along the 15 mm × 60 mm specimen, which is accounted for during the intensity normalization procedure with the help of the measured local transmission of the specimen. The specimen was scanned by the X-ray beam with a step of 0.5 mm, each time recording a 0.5s image. After correction of the detector distortions

(dark current, flat-field, grid distortions), normalization and subtraction of the background noise, the corrected 2D intensity could be used as such or radially averaged to obtain an average intensity as a function of the scattering vector q. Details on the interpretation of the SAXS intensity will be given further in the paper.

Specimens for transmission electron microscopy (TEM) were prepared by mechanically grinding the transverse slice to a thickness of about 100 µm and punching 3 mm discs from the regions of interest, as defined after SAXS observations (i.e. base material far away from the weld centre and the thermo-mechanically affected zone where precipitates thickening occur (see further in the paper)). The TEM foils were then prepared through standard twin-jet electropolishing using 1/3 nitric acid in methanol at −20 °C. The TEM observations were performed on a JEOL 3010, operating at 300 kV.

TEM observations

A bright field transmission electron micrograph of the base material is shown in Figure 1(a) together with the corresponding diffraction pattern as an inset (viewing direction ⟨1 1 0⟩). This TEM micrograph confirms that the microstructure is composed essentially of very thin T_1 precipitates. Two variants out of 4 are parallel to the zone axis and show as streaking in the directions normal to their habit planes on the diffraction pattern. The base material consists in a fine dispersion of thin T_1 precipitates homogeneously distributed within the grains. Figure 1(b) is a bright field TEM micrograph obtained in the thermo-mechanically affected zone, in a zone which will be identified further in the paper as a zone containing thicker precipitates (viewing direction ⟨1 1 2⟩). In this zone axis, only 1 variant of T_1 appears edge on. Here again, the microstructure consists of T_1 precipitates homogeneously distributed, albeit of different length, thickness and volume fraction than in the base material.

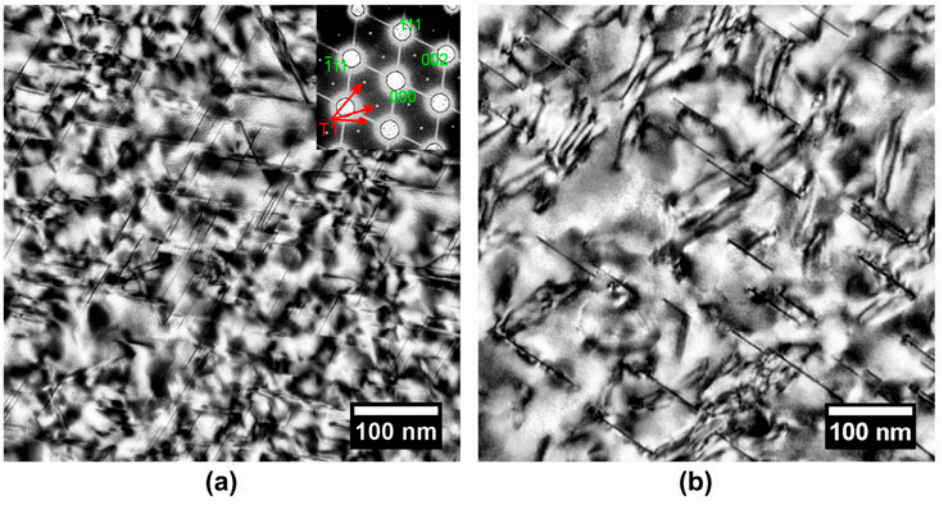

Figure 1. (colour online) TEM observations: (a) bright field of the base material in the ⟨1 1 0⟩ viewing direction (2 variants of T_1 are observed as thin lines, as confirmed by diffraction pattern, inset) and (b) bright field obtained in the TMAZ in the ⟨1 1 2⟩ viewing direction (1 variant of T_1 is observed).

In the weld nugget, the situation is completely different (Figure 2). Both on the bright field or on the diffraction pattern (not shown here), no indication of T_1, θ' nor δ' precipitates. It is unsure from these observations if smaller clusters and/or GP zones are present at this stage, but no indications were found on the diffraction pattern. Coarse particles are observed. As they can also be found in the base material, they are most likely Mn-bearing dispersoids and pre-existed the FSW process. From these TEM observations, it seems reasonable to assume that the FSW process has dissolved the dominating T_1 precipitates.

SAXS mapping of the FSW weld

In order to map the precipitates microstructure of the welded structure, we have performed a regular scanning of a transverse section of the weld with the X-ray beam, recording a SAXS image for each position. The grid step was chosen to be 0.5 mm. The complete map consists in 3360 images (roughly 15 mm × 50 mm). Figure 3 is a mosaic made of a subset of all the SAXS images (1 image every 2 mm is shown). The first general observation is that the SAXS signal is generally not isotropic. This is not surprising since (1) the expected phases are mostly non-spherical, (2) a rolling texture is expected in these aluminium plates and (3) the grain size is of the same order of magnitude than the beam size (so that the situation is far from a "powder like" sample).

In the case of a constant known texture, the plate-like T_1 precipitates in well-defined habit planes give rise to the star patterns, which are observed in the base material (see images away from the centre in Figure 3). Those can be interpreted using our recent protocol [22], and both the thickness and the length of the precipitates can be extracted for precipitates as thin as ~1 nm and as long as ~100 nm. However, this protocol is unpractical in the present situation because of the inhomogeneity of the texture across the weld structure, with the extreme case of the weld nugget where recrystallization took place. Visual inspection of the 2D images shown in Figure 3 clearly indicates that the microstructure of the weld centre is very different than that of the base material. The signal at the centre is much more isotropic, which seems at first consistent with

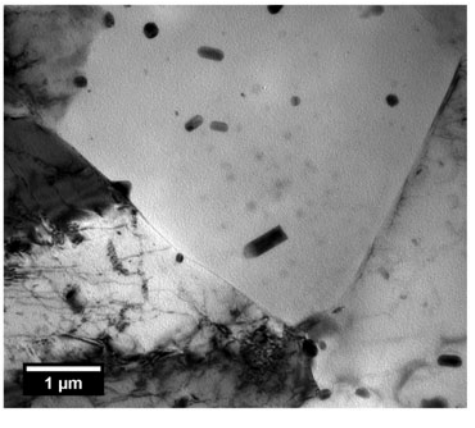

Figure 2. Bright field TEM observation of the weld nugget in the ⟨1 1 0⟩ direction.

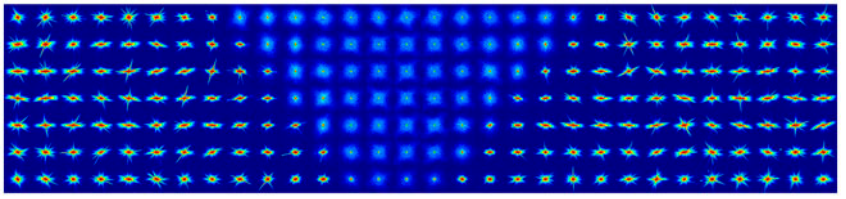

Figure 3. (colour online) Mosaic of 210 out of the 3360 recorded SAXS images (covering a 15 mm × 60 mm. The weld centre clearly shows a different type of pattern than the based material.

recrystallization of the weld nugget; however, the spatial zone where this happens is more extended that the recrystallized weld nugget. The origin of the more diffuse SAXS patterns should thus be the precipitates themselves, which, if not spherical, should at least have a much smaller aspect ratio than the T_1 of the base material.

Although the SAXS patterns are visually not isotropic, we assumed that they could be treated as such and radially averaged to obtain a $I(q)$ plot. We will justify this assumption a posteriori based on the expected features of this plot for the base material. If we assume a cylindrical shape for the precipitates, with diameter D and thickness ε and a direction normal to the platelet making an angle φ with thescattering vector, we get the SAXS intensity by integrating over all φ directions so that [29,30]:

$$I(q) = \int_0^{\pi/2} \Delta\rho^2 n_v V^2 \left| \frac{\sin(\frac{q\varepsilon}{2}\cos\varphi)}{\frac{q\varepsilon}{2}\cos\varphi} \right|^2 \left| \frac{2J_1(\frac{qD}{2}\sin\varphi)}{\frac{qD}{2}\sin\varphi} \right|^2 d\varphi \tag{1}$$

$\Delta\rho^2$ is the electronic density contrast between matrix and precipitates, η_v is the precipitates number density, $V = \frac{\pi D^2 \varepsilon}{4}$ is the volume of a precipitate and J_1 is the Bessel function of the first kind of order 1. Equation (1) cannot be calculated analytically, but in the case where $D \gg \varepsilon$, 2 interesting approximations can be made. First, in the Guinier regime where $\frac{qD}{2} \ll 1$, the term in ε can be considered constant. The term in D can be expressed by developing the intensity as a Guinier exponential with $Rg^2 = \frac{1}{8}D^2$. This corresponds to values of $q \ll \frac{2}{D}$ which, if we consider the diameter of T_1 precipitates in Figure 1, are in the range 10^{-3}Å^{-1} and less. These values are not covered by the experimental setup so that the length of the precipitates cannot be known precisely only through the SAXS experiments.

If $\frac{qD}{2} \gg 1$, the Bessel function will vary *much* more rapidly in φ than the sine function, and it will take non-negligible values only in the vicinity of $\varphi = 0$. This enables to take the sine term out of the integral and which can then be performed analytically. The intensity now reads:

$$I(q) = \Delta\rho^2 n_v V^2 \left(\frac{\sin(\frac{q\varepsilon}{2})}{\frac{q\varepsilon}{2}} \right)^2 \frac{8}{q^2 D^2} \tag{2}$$

And finally

$$I(q) = \Delta\rho^2 f_v \frac{2\pi\varepsilon}{q^2} \left(\frac{\sin(\frac{q\varepsilon}{2})}{\frac{q\varepsilon}{2}} \right)^2 \tag{3}$$

or, for $qD \gg 1$ and $q\varepsilon \ll 1$

$$I(q) \approx \Delta\rho^2 f_v \frac{2\pi\varepsilon}{q^2} e^{-\frac{q^2\varepsilon^2}{12}} \tag{4}$$

with $f_v = n_v V$, the volume fraction of particles. This equation shows that in an intermediate range (i.e. for q between $2/D$ and $1/\varepsilon$), the SAXS intensity of a flat platelet should exhibit a $1/q^2$ behaviour, the classical signature of a flat particle [30]. It is interesting to note that, since we have introduced the precipitate volume fraction, the precipitates diameter (experimentally out of reach) does not appear explicitly in Equation (3) anymore. If Equation (3) applies (i.e. if the signal arises from flat precipitates with a distribution which can be considered as isotropic), fitting of the signal gives both the thickness of the particles and the relative volume fraction (if the electronic contrast is unknown).

Figure 4 shows the radially averaged SAXS intensity for 3 typical SAXS images. Both in the base material and in the HAZ, the intensity shows the $1/q^2$ signature of platelet particles, which justifies a posteriori the assumption of the model, as we know the type of precipitates in the base material (Figure 1(a)). In the weld centre, however, the signal consists in a low q $1/q^4$ Porod behaviour originating from large particles and a small particles contribution. The low q contribution originates at least partly from the large precipitates observed in Figure 2, and the large q contribution confirms that, although no nanometric precipitates can be observed by TEM in the nugget, clusters and/or GP zones are present at this stage. From Figure 4, it is evident that the q-range is sufficient to observe these very small precipitates but does not allow for a precise description of the asymptotic behaviour so that a distinction between spheroidal clusters and plate-like GP zones is not possible. We have not made the distinction and treated all the small precipitates as a distribution of spherical clusters.

As seen in Figure 4, the SAXS pattern can be interpreted either as platelet particles, or as the sum of a low q Porod contribution originating from large particles and the contribution of clusters and/or GP zones. The complete SAXS mapping has been

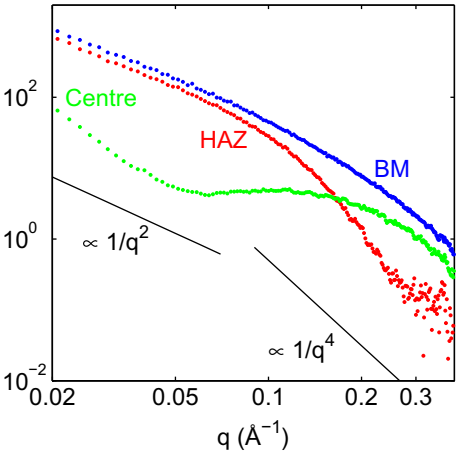

Figure 4. (colour online) Typical SAXS patterns of base material (BM), heat-affected zone (HAZ) and weld centre. The HAZ and BM spectra present a $1/q^2$ behaviour typical of flat particle form factor.

processed by fitting the signal at each point by the sum of 3 contributions: a low q Porod contribution, spherical clusters and platelet particles.

The results of the fit are microstructure maps shown in Figures 5 and 6. Figure 5 shows the size and volume fraction of clusters. It is evident that clusters are only present at the centre of the weld structure. The size distribution of clusters is very narrow, ranging between 6 and 8 Å in radius. There is a significant gradient of volume fraction, in particular from top to bottom, the higher fraction being found at the top. The domain of existence of the clusters is significantly larger than the recrystallized weld nugget, the outline of which can in fact be distinguished both in Figure 5(a) and (b). The thermo-mechanical history of the samples originates in subtle variations in the clusters size and fraction which are visible on the SAXS maps.

The T_1 platelet precipitates contribution is shown in Figure 6. Figure 6(a) maps the thickness of the precipitates, highlighting a constant thickness in the base material, compatible with single thickness T_1 precipitates. Closer from the weld centre, the precipitates have thicken on a thin layer together with a partial dissolution, as confirmed by the volume fraction map of Figure 6(b). The volume fraction map shows the weld

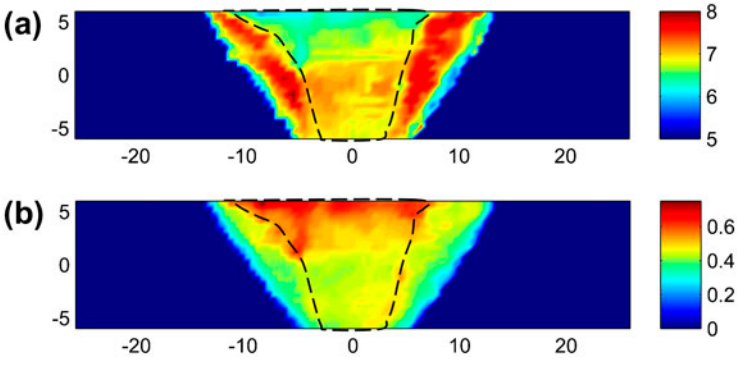

Figure 5. (colour online) SAXS mapping of the clusters. (a) radii (Å) and (b) volume fractions (A.U.) The outline of the recrystallized weld nugget is shown as a dashed line.

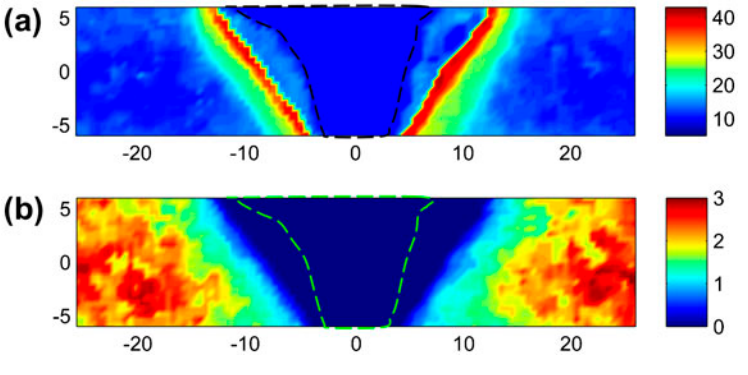

Figure 6. (colour online) SAXS mapping of the T_1 precipitates. (a) thickness (Å) and (b) volume fractions (A.U.) The outline of the recrystallized weld nugget is shown as a dashed line.

centre zone where the T_1 precipitates have completely disappeared, which correlates well with the zone of existence of the clusters of Figure 5.

To confirm the existence of the layer of thickened precipitates in the thermo-mechanically affected zone, we have prepared a TEM thin foil in this area, as guided by the SAXS results. The TEM bright field was shown in Figure 1(b). Although no quantitative thickness measurement can be extracted from this bright field image, comparison between Figure 1(a) and (b) gives a qualitative confirmation of the partial dissolution of the T_1 precipitates together with a thickening of the precipitates.

To correlate this precipitate microstructure characterization with the mechanical properties, we have performed a microhardness mapping of the weld structure on the same scale as the SAXS microstructure mapping. The results are shown in Figure 7. It shows that the hardness is relatively constant in the base material, close to 175 HV, and drops at the weld centre to a value of about 120–125 HV. The spatial correspondence between Figures 7 and 6(b) demonstrates a good correlation between the T_1 precipitation state and the microhardness, which is further confirmed by Figure 8, where both the volume fraction and the hardness are plotted along a line situated at mid-thickness of the plate.

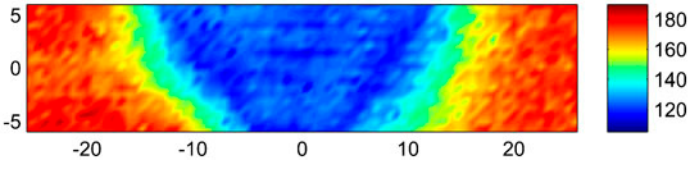

Figure 7. (colour online) Microhardness mapping (HV).

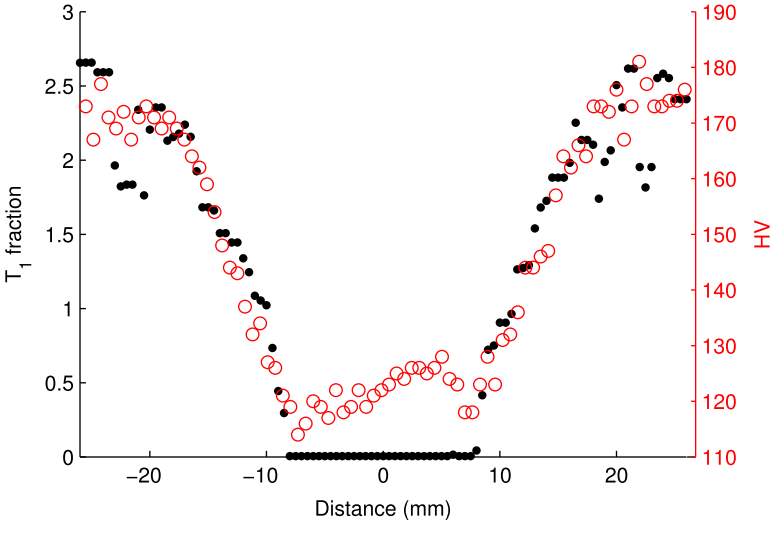

Figure 8. (colour online) Volume fraction of T_1 precipitates (black dots) and microhardness (red circle) along a mid-thickness line across the weld, highlighting the correlation.

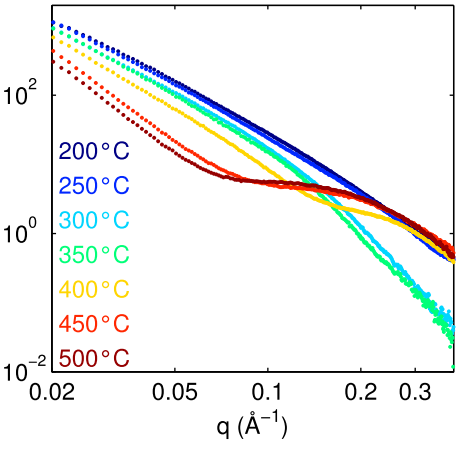

Figure 9. (colour online) SAXS patterns of (a) T8 samples and (b) T3 samples subjected to 5 s heat treatment in a salt bath at different temperatures ranging between 200 and 500 °C.

Discussion

To further understand the microstructure evolution during the FSW process, we have performed a series of heat treatments aiming at mimicking the temperature exploration during the FSW process. One millimetre thick plates of the base alloy in the T8 state were heat treated in a salt bath for 5 s at different temperature ranging between 200 and 500 °C, followed by a rapid water quench and a few days of natural ageing. SAXS samples were then prepared and SAXS images recorded in order to compare to those obtained on the FSW welded structure.

The resulting SAXS profiles are shown in Figure 9 and can be directly compared with the SAXS signal of the BM, HAZ and weld centre from Figure 4 and allow for an estimate of the temperature reached in each zone. It appears that the 200 and 250 °C are both similar to the base material signal, indicating that a short stay at temperature below 250 °C should not modify the precipitates microstructure. The 300 and 350 °C signals are much closer to that of the HAZ where the precipitates have started to coarsen and partially dissolve. Above 400 °C, it appears that there is no T_1 left and the signal is close to that of the weld centre, originating from clusters/GP zones. It is interesting to notice that an adequate mimicking of the weld process in terms of microstructure evolution can be performed by 5s heat treatments. It suggests that only the temperature excursion is responsible for the final microstructure and that the strong straining resulting in recrystallization of the nugget and to a mechanically affected zone has only marginal effect on the distribution of the precipitates (although there are some subtle differences in the clusters distribution in and out of the nugget). This is of particular interest for the application of precipitation model to the FSW process of this alloy.

Summary

We have mapped the heterogeneous precipitates microstructure issued from the friction stir welding of a 2050 Al–Li–Cu alloy in the T8 temper. We have shown that the FSW

process has dissolved the existing T_1 precipitates in a zone, which covers a broader zone than the weld nugget. Where the temperature has not reached the dissolution temperature (about 450 °C), the remaining T_1 precipitates have partially dissolved and have undergone a significant thickening. In T_1 free zone, small clusters and/or GP zones have formed at room temperature after the welding process. The temperature elevation alone is shown to explain those precipitate variations, the large strains having apparently only little, if any, influence. Comparison between microstructure and microhardness mapping has provided evidence that there is a strict correlation between the volume fraction of the T_1 precipitates and the hardness of the material.

Acknowledgements

This work was financially supported by the ANR MatetPro program (ANR-08-MAPR-0020-05 "CORALIS"). The authors would like to thank the staff at D2AM-BM02 CRG beamline at ESRF.

References

[1] R.S. Mishra and Z.Y. Ma, Mater. Sci. Eng. R Rep. 50 (2005) p.1.
[2] T. Warner, Recently-Developed Aluminum Solutions for Aerospace Applications, in: Mater. Sci. Forum, Vol. 519, 2006.
[3] F. Gayle, F. Heubaum and J. Pickens, J. Scr. Metall. Mater. 24 (1990) p.79.
[4] R.A. Herring, F.W. Gayle and J.R. Pickens, J. Mater. Sci. 28 (1993) p.69.
[5] B. Decreus, A. Deschamps, F. De Geuser, P. Donnadieu, C. Sigli and M. Weyland, Acta Mater. 61 (2013) p.2207.
[6] B.M. Gable, A.W. Zhu, A.A. Csontos and E.A. Starke, J. Light Met. 1 (2001) p.1.
[7] J.F. Nie and B.C. Muddle, Mater. Sci. Eng. A 319 (2001) p.448.
[8] S.C. Wang and M.J. Starink, Int. Mater. Rev. 50 (2005) p.193.
[9] P. Donnadieu, Y. Shao, F. De Geuser, G.A. Botton, S. Lazar, M. Cheynet, M. de Boissieu and A. Deschamps, Acta Mater. 59 (2011) p.462.
[10] C. Dwyer, M. Weyland, L.Y. Chang and B.C. Muddle, Appl. Phys. Lett. 98 (2011) p.201909.
[11] N.D. Alexopoulos, E. Migklis, A. Stylianos and D.P. Myriounis, Int. J. Fatigue 56 (2013) p.95.
[12] A. Astarita, A. Squillace, E. Armentani and S. Ciliberto. Metall. Ital. (2012) p.31.
[13] C. Bitondo, U. Prisco, A. Squilace, P. Buonadonna and G. Dionoro, Int. J. Adv. Manuf. Technol. 53 (2011) p.505.
[14] P. Cavaliere, M. Cabibbo, F. Panella and A. Squillace, Mater. Ds. 30 (2009) p.3622.
[15] Y.E. Ma and P. Irving, J. Aircr. 48 (2011) p.1238.
[16] Y.E. Ma, Z. Zhao, B. Liu and W. Li, Mater. Sci. Eng. A 569 (2013) p.41.
[17] Y.E. Ma, B. Liu and Z. Zhao, Appl. Mech. Mater. 138–139 (2011) p.651.
[18] M Yu'e, W. Zhenhai, *Fatigue Behaviour in Friction Stir Welded 2198-T8 Al-Li Alloy Joint for Integral Metal Fuselage Application*, 2010.
[19] R.W. Fonda and J.F. Bingert, Metall. Mater. Trans A 37 (2006) p.3593.
[20] A.K. Shukla and W.A. Baeslack III, Scr. Mater. 56 (2007) p.513.
[21] A.K. Shukla and W.A. Baeslack, Sci. Technol. Weld. Join. 14 (2009) p.376.
[22] F. De Geuser, F. Bley and A. Deschamps, J. Appl. Crystallogr. 45 (2012) p.1208.
[23] D.L. Chen and M.C. Chaturvedi, Metall. Mater. Trans A 32 (2001) p.2729.

[24] A. Steuwer, M. Dumont, J. Altenkirch, S. Birosca, A. Deschamps, P.B. Prangnell and P.J. Withers, Acta Mater. 59 (2011) p.3002.
[25] M. Dumont, A. Steuwer, A. Deschamps, M. Peel and P.J. Withers, Acta Mater. 54 (2006) p.4793.
[26] F. De Geuser, F. Bley, A. Denquin and A. Deschamps, J. Phys. Conf. Ser. 247 (2010) p.012034.
[27] P. Lequeu, K.P. Smith and A. Daniélou, J. Mater. Eng. Perform 19 (2009) p.841.
[28] G. Pouget and A.P. Reynolds, Int. J. Fatigue 30 (2008) p.463.
[29] A. Guinier and G. Fournet, *Small-Angle Scattering of X-Rays*, John Wiley & Sons, New York, 1955.
[30] G. Porod, *General Theory*, in *Small-Angle X-ray Scatt*, O. Glatter and O. Kratky, eds., Academic Press, London, 1982.